



## Research Paper

**Magnetic  $\text{Fe}_2\text{O}_3$ /mesoporous black  $\text{TiO}_2$  hollow sphere heterojunctions with wide-spectrum response and magnetic separation**

Bojing Sun, Wei Zhou\*, Haoze Li, Liping Ren, Panzhe Qiao, Fang Xiao, Lei Wang, Baojiang Jiang, Honggang Fu\*

Key Laboratory of Functional Inorganic Material Chemistry, Ministry of Education of the People's Republic of China, Harbin Institute of Technology Shenzhen Graduate School, Shenzhen 518055, PR China



## ARTICLE INFO

**Keywords:**

Mesoporous black  $\text{TiO}_2$  hollow sphere  
Wide-spectrum response  
Magnetic separation  
Heterojunction  
Solar-driven photocatalysis

## ABSTRACT

The solar-light-harvesting and separation of nanostructured photocatalysts in slurry systems are key issues in fields of photocatalysis. Herein, magnetic  $\text{Fe}_2\text{O}_3$ /mesoporous black  $\text{TiO}_2$  heterojunctions ( $\text{M}-\text{Fe}_2\text{O}_3/\text{b}-\text{TiO}_2$ ) are fabricated through wet-impregnation and surface hydrogenation strategy, which show wide-spectrum response and magnetic separation. The decreased specific surfaces, pore sizes and pore volumes from  $\sim 80$  to  $67 \text{ m}^2 \text{ g}^{-1}$ ,  $\sim 12$  to  $10.3 \text{ nm}$ , and  $\sim 0.20$  to  $0.16 \text{ cm}^3 \text{ g}^{-1}$ , respectively, all confirm the efficient loading of magnetic  $\text{Fe}_2\text{O}_3$ . The  $\text{M}-\text{Fe}_2\text{O}_3/\text{b}-\text{TiO}_2$  with narrow bandgap of  $\sim 2.41 \text{ eV}$  extends the photoresponse from UV to near infrared region and exhibits excellent solar-driven photocatalytic degradation performance and long-term stability for complete mineralization methyl orange and high-toxic herbicide metribuzin. The photocatalytic reaction apparent rate constant  $k$  for metribuzin is  $\sim 9$  times higher than that of pristine  $\text{TiO}_2$  under AM 1.5 irradiation. Especially for single-wavelength of  $950 \text{ nm}$ , the degradation ratio is up to 4%. The enhancement is attributed to  $\text{Ti}^{3+}$  and magnetic  $\text{Fe}_2\text{O}_3$  with narrow bandgap facilitating solar-light-harvesting, the hollow structure benefiting mass transport, and the heterojunctions favoring the spatial separation of photo-generated electron-hole pairs. The magnetic separation is conducive to recycle of photocatalysts, which favors practical applications in environment.

## 1. Introduction

With the fast development of the textile industry, lots of industrial sewage spread poisonous chemicals into soil and water resources [1–3]. The pollution of water with agrochemical can pose a significant destruction to aquatic ecosystems and drinking water resources [4–7]. What is worse, the triazine compounds have been the most widely used pesticides in recent decades, which bring about insurmountable environmental problems [8,9]. The photocatalytic oxidation, as one of the green technologies that have advantages of high-efficiency, non-selective oxidation, and low-cost, has been recognized as an important and effective candidate to remove the toxic and harmful contaminants in aqueous environment [10–14]. Titanium dioxide ( $\text{TiO}_2$ ) is one of the most important photocatalysts due to its cheapness, excellent physical and chemical stability and high efficiency [15,16]. However, the large bandgap ( $\sim 3.2 \text{ eV}$ ) for anatase  $\text{TiO}_2$  limits its utilization ratio of solar energy [17,18]. Although some approaches including metal and non-metal doping were used for narrowing the bandgap of  $\text{TiO}_2$ , the visible-light-driven photocatalytic performance and long-term stability are unsatisfactory [19,20]. Fortunately, Chen and coworkers discovered

black  $\text{TiO}_2$  nanomaterials via surface hydrogenation strategy recently, which narrowed the bandgap and extended the photoresponse from ultraviolet to visible light and/or near infrared region [21]. The excellent solar-driven photocatalytic performance represented a breakthrough for wide-spectrum response  $\text{TiO}_2$  materials. Since then, numerous efforts have been made to synthesize various black  $\text{TiO}_2$  nanomaterials and the visible-light-driven photocatalytic performance is indeed improved obviously [22,23].

So far, the separation of nanostructured photocatalysts in slurry systems is a difficult subject which needs to be solved urgently. Although some approaches, such as centrifugation, sedimentation and vacuum filtration, have been adopted, the separation effectiveness of photocatalysts is not satisfactory [24,25]. Magnetic separation may be a good choice for their separation, because the magnetic photocatalysts can be separated easily when the applied magnetic field appears. Of various magnetic materials, magnetic ferric oxide ( $\text{Fe}_2\text{O}_3$ ) has drawn the most attention due to its earth-abundant, low-cost, excellent ferromagnetism, narrow bandgap and high chemical and physical stability [26,27]. The narrowed bandgap of  $\sim 2.24 \text{ eV}$  could extend the photoresponse to visible light region [28]. Therefore, magnetic  $\text{Fe}_2\text{O}_3$  is a

\* Corresponding authors.

E-mail addresses: [zwchem@hotmail.com](mailto:zwchem@hotmail.com) (W. Zhou), [fuhg@hit.edu.cn](mailto:fuhg@hit.edu.cn), [fuhg@vip.sina.com](mailto:fuhg@vip.sina.com) (H. Fu).

good candidate for efficient absorption of long-wavelength light and magnetic separation. Some strategies have been taken for synthesizing magnetic  $\text{Fe}_2\text{O}_3/\text{TiO}_2$  composites, which represented excellent separation effect [29–31]. However, the low quantum efficiency for traditional  $\text{TiO}_2$  material is still beyond the requirement for practical applications. Mesoporous black  $\text{TiO}_2$  hollow spheres would be ideal candidates for further improving the solar-driven photocatalytic performance because the unique hollow structures are beneficial for efficient light utilization and offering good hosts to load magnetic  $\text{Fe}_2\text{O}_3$ . Therefore, to fabricate magnetic  $\text{Fe}_2\text{O}_3$ /mesoporous black  $\text{TiO}_2$  hollow sphere heterojunctions will satisfy the requirement of both wide-spectrum response and magnetic separation simultaneously.

Herein, we demonstrate a facile wet-impregnation and surface hydrogenation route to synthesize magnetic  $\text{Fe}_2\text{O}_3$ /mesoporous black  $\text{TiO}_2$  hollow sphere heterojunctions. The resultant heterojunctions are considered as photocatalysts with wide-spectrum response and magnetic separation, which exhibit excellent solar-driven photocatalytic performance and long-term stability for complete mineralization methyl orange and metribuzin. The novel magnetic heterojunctions photocatalysts will have widespread practical applications in environmental fields.

## 2. Experimental section

### 2.1. Chemicals

*N,N*-dimethylformamide (DMF), ethanol (EtOH), ethylenediamine, ferric nitrate ( $\text{Fe}(\text{NO}_3)_3 \cdot 9\text{H}_2\text{O}$ ), methanol and potassium hydroxide (KOH) were of analytical grade and purchased from Tianjin Kemiou Chemical Reagent Co., Ltd. Tetrabutyltitanate (TBOT), hydroxylammonium chloride, sulfanilic acid, 1-naphthylamine and anhydrous oxalic acid were purchased from Aladdin Industrial Inc. All chemicals were used as received without further purification. Deionized water was used for all experiments.

### 2.2. Synthesis of magnetic $\text{Fe}_2\text{O}_3$ /mesoporous black $\text{TiO}_2$ hollow sphere heterojunctions

The synthesis of mesoporous black  $\text{TiO}_2$  hollow spheres was according to literature [32]. The preparation of magnetic  $\text{Fe}_2\text{O}_3$ /mesoporous black  $\text{TiO}_2$  hollow sphere heterojunctions was through wet-impregnation and surface hydrogenation route. Typically, different amounts of  $\text{Fe}(\text{NO}_3)_3 \cdot 9\text{H}_2\text{O}$  and 100 mg of  $\text{TiO}_2$  hollow spheres were mixed evenly in 30 mL ethanol to form a mixed solution. The mixture was stirred for 6 h at room temperature and then dried at 60 °C in oven overnight. Finally, the samples were calcined at 400 °C for 5 h in Air, with a temperature ramping rate of 5 °C min<sup>-1</sup>. Before being calcined in a  $\text{H}_2$  flow at 200 °C for 3 h under normal pressure conditions with a constant heating rate of 10 °C min<sup>-1</sup>, the samples were deaerated under an inert gas flow ( $\text{N}_2$ ) for 0.5 h. The resultant materials were denoted as M- $\text{Fe}_2\text{O}_3/b\text{-TiO}_2$ . The loading amounts of  $\text{Fe}_2\text{O}_3$  were testified to be 9, 13, 16, 19 and 24%, respectively, according to Inductively Coupled Plasma (Optima 8300 (PerkinElmer, USA) ICP-OES). To provide a comparison with the M- $\text{Fe}_2\text{O}_3/b\text{-TiO}_2$  sample, magnetic  $\text{Fe}_2\text{O}_3$ /mesoporous black  $\text{TiO}_2$  hollow sphere heterojunctions was also synthesized under the same conditions without the  $\text{H}_2$  calcined (denoted as M- $\text{Fe}_2\text{O}_3/\text{TiO}_2$ ).

### 2.3. Characterization

X-ray diffraction (XRD) patterns was performed on a Bruker D8 Advance diffractometer by using Cu  $\text{K}\alpha$  radiation ( $\lambda = 1.5406 \text{ \AA}$ , 40 kV, 40 mA). Raman measurements were obtained with a Jobin Yvon HR 800 micro-Raman spectrometer at 457.9 nm. The laser beam was focused with a 50 objective lens to a ca. 1  $\mu\text{m}$  spot on the surface of the sample. Scanning electron microscopy (SEM) using a Hitachi S-4800

instrument operated at 15 kV. The transmission electron microscopy (TEM) experiments were obtained on a JEOL JEM-2100 electron microscope (JEOL, Japan) with an acceleration voltage of 200 kV. Carbon-coated copper grids were used as sample holders. X-ray photoelectron spectroscopy (XPS, Kratos, ULTRA AXIS DLD) was recorded to study the surface states with monochromic Al  $\text{K}\alpha$  (1486.6 eV) radiation. All binding energies were calibrated by referencing to C 1speak at 284.6 eV. UV/vis adsorption spectra were conducted on a UV/vis spectrophotometer (Lambda 950 (PerkinElmer, USA)) in the range of 200–1800 nm, with fine  $\text{BaSO}_4$  powders as reference. The bandgaps were estimated by extrapolating a linear part of the plots to  $(\alpha h\nu)^2 = 0$ . Nitrogenadsorption-desorption isotherms at 77 K were collected on anAUTOSORB-1 (Quantachrome Instruments) nitrogen adsorption apparatus. All samples were degassed under vacuum at 180 °C for at least 8 h before measurement. The Brunauer–Emmett–Teller (BET) equation was used to calculate the specific surface area. Pore-size distribution was measured from the adsorption branch of the isotherm using the Barrett–Joyner–Halenda (BJH) method from the adsorption branch of the isotherms. The magnetic hysteresis loops were made by a LakeShore 7404 (USA) vibrating sample magnetometer (VSM).

### 2.4. Photocatalytic activity

Photocatalytic test was evaluated by the photocatalytic decomposition of methyl orange (MO) and metribuzin ( $\text{C}_8\text{H}_{14}\text{N}_4\text{OS}$ ) under AM 1.5 irradiation. The light intensity was calibrated to 100 mW cm<sup>-2</sup> before measurement. In a typical experiment, the photocatalyst (50 mg) was added to 100 mL metribuzin solution (10 mg L<sup>-1</sup>) or MO solution (10 mg L<sup>-1</sup>). The suspension was irradiated with a 300 W Xe lamp equipped with an AM 1.5 filter. To confirm the stability of the photocatalysts, we recycled the catalysts after experiments by deionized water and ethanol cleaning several times, and then drying at 60 °C for 6 h to remove the residual reactants and reactivate the adsorption and catalytic performance. The residual MO and metribuzin concentration was analyzed by total organic carbon (TOC, TOC-VCPN (SHIMADZU) analyser). The single wavelength efficiency was performed using metribuzin solution (0.1 mg L<sup>-1</sup>). Before irradiation, the suspensions were magnetically stirred in the dark for 20 min to establish adsorption/desorption equilibrium between the organic and the surface of the catalyst at room temperature. The single-wavelength efficiency was irradiated with a 300 W Xe lamp with a bandpass filter (365, 420, 520 and 950 nm) system.

### 2.5. Photoelectrochemical measurement

Photoelectrochemical properties were investigated using a Princeton Versa STAT 3 in a standard three electrode configurations with M- $\text{Fe}_2\text{O}_3/b\text{-TiO}_2$  and  $\text{TiO}_2$  materials used as photoanodes, Pt foil as the counter electrode, an Ag/AgCl reference electrode in home-built crystal equipment containing 1 M KOH solution. The KOH solution was purged with  $\text{N}_2$  and used as the electrolyte. The photoanodes were prepared by an easy spray coating method, using a glass-rod to roll a paste containing 30 mg of powders and 2 mL of EtOH on a transparent FTO glass-substrate with an effective diaphragm area 1 cm<sup>2</sup> (TCO, fluorine doped  $\text{SnO}_2$  layer, 20 Ω/square, Nippon sheet glass, Japan), followed by calcining 120 min at 400 °C under a  $\text{N}_2$  atmosphere with a constant heating rate of 5 °C min<sup>-1</sup>. An AM 1.5 power system (Oriel, USA) was used as the light irradiation source.

## 3. Results and discussion

### 3.1. Crystal structure and morphology of M- $\text{Fe}_2\text{O}_3/b\text{-TiO}_2$ heterojunctions

After surface hydrogenation, the X-ray diffraction (XRD) patterns of both M- $\text{Fe}_2\text{O}_3/\text{TiO}_2$  and M- $\text{Fe}_2\text{O}_3/b\text{-TiO}_2$  heterojunctions (Fig. 1A) show five obvious crystal peaks at  $2\theta = 25.2\text{--}55.2^\circ$ , which could be

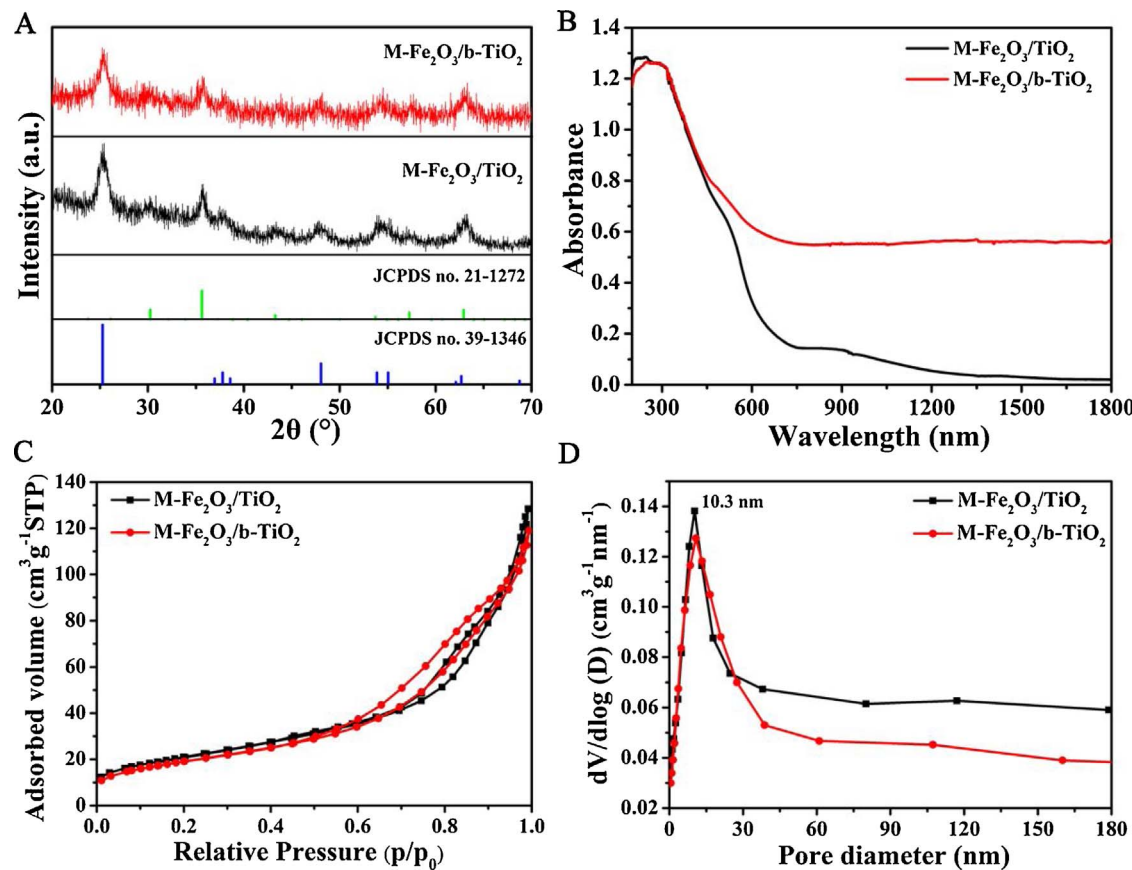


**Fig. 1.** Typical XRD patterns (A), ultraviolet-visible absorption spectra (B),  $\text{N}_2$  adsorption-desorption isotherms (C) and the corresponding Barrett-Joyner-Halenda (BJH) pore size distribution plots (D) of  $\text{M-Fe}_2\text{O}_3/\text{TiO}_2$  and  $\text{M-Fe}_2\text{O}_3/\text{b-TiO}_2$  heterojunctions, respectively.

ascribed to the anatase phase (JCPDS no. 21-1272). The crystal peaks at  $2\theta = 35.56$  and  $62.76^{\circ}$  proves the existence of maghemite phase of  $\text{M-Fe}_2\text{O}_3$  (JCPDS no. 39-1346). The results confirm the efficient assembly of  $\text{M-Fe}_2\text{O}_3$  and  $\text{TiO}_2$ . However, the intensity of both  $\text{M-Fe}_2\text{O}_3$  and  $\text{TiO}_2$  for  $\text{M-Fe}_2\text{O}_3/\text{b-TiO}_2$  heterojunctions decreases and broadens obviously, illustrating that their crystalline structures have some variation after surface hydrogenation. Fig. 1B shows the absorption of  $\text{M-Fe}_2\text{O}_3/\text{TiO}_2$  and  $\text{M-Fe}_2\text{O}_3/\text{b-TiO}_2$  heterojunctions, which exhibits an obvious redshift in the onset of absorption from the UV to near infrared region (up to 1800 nm). This is ascribed to the efficient surface hydrogenation. It is very interesting to note that the absorption in visible light and near infrared region for  $\text{M-Fe}_2\text{O}_3/\text{b-TiO}_2$  heterojunctions is stronger than that of  $\text{M-Fe}_2\text{O}_3/\text{TiO}_2$ , indicating the surface hydrogenation indeed favoring the light harvesting. Diffuse reflect measurements reveal that the bandgap is reduced for  $\text{M-Fe}_2\text{O}_3/\text{TiO}_2$  ( $\sim 2.59$  eV) after loading  $\text{M-Fe}_2\text{O}_3$  with narrow bandgap (Fig. S1). After surface hydrogenation, the bandgap of  $\text{M-Fe}_2\text{O}_3/\text{b-TiO}_2$  heterojunctions further reduced to  $\sim 2.41$  eV, which may substantially enhance the solar-driven degradation efficiency [33].  $\text{N}_2$  adsorption-desorption isotherms of  $\text{M-Fe}_2\text{O}_3/\text{TiO}_2$  and  $\text{M-Fe}_2\text{O}_3/\text{b-TiO}_2$  heterojunctions both show typical type IV curves, indicating mesoporous materials, as shown in Fig. 1C and D. The Brunauer–Emmett–Teller surface area, pore size and pore volume of  $\text{M-Fe}_2\text{O}_3/\text{b-TiO}_2$  heterojunctions are  $\sim 67 \text{ m}^2 \text{ g}^{-1}$ , 10.3 nm and  $0.16 \text{ cm}^3 \text{ g}^{-1}$ , respectively. The pore size and pore volume of  $\text{M-Fe}_2\text{O}_3/\text{b-TiO}_2$  heterojunctions are both smaller than that of black  $\text{TiO}_2$  hollow spheres (12 nm,  $0.2 \text{ cm}^3 \text{ g}^{-1}$ ) [32], indicating the efficient loading of  $\text{M-Fe}_2\text{O}_3$  on mesoporous black  $\text{TiO}_2$  hollow spheres.

The scanning electron microscopy (SEM) and transmission electron microscopy (TEM) images both show mesoporous  $\text{M-Fe}_2\text{O}_3/\text{b-TiO}_2$  hollow spheres with diameters of  $\sim 700$  nm before and after hydrogenation (Fig. 2A–C). The mesopores can also be observed from Fig. 2C,

indicating that the mesostructure is still existed after loading  $\text{M-Fe}_2\text{O}_3$ , which is beneficial for the diffusion of reactants and products. Compared to mesoporous black  $\text{TiO}_2$  hollow spheres, the wall thickness increases from 65 to 70 nm (Fig. S2), further demonstrating the efficient loading of  $\text{M-Fe}_2\text{O}_3$ . The HRTEM image (Fig. 2D, E) clearly shows that the pore walls consist of highly crystalline  $\text{TiO}_2$  nanoparticles and covering  $\text{M-Fe}_2\text{O}_3$  nanoparticles. Lattice fringes with a d-spacing of 0.35 nm are clearly observed, which correspond well to the (101) crystallographic planes of anatase. Another d-spacing of 0.295 nm correspond to  $\text{M-Fe}_2\text{O}_3$  (311) plane. As shown in Fig. 2D and E,  $\text{M-Fe}_2\text{O}_3$  is not only loaded on the outer surface (Fig. 2D) of the  $\text{TiO}_2$  hollow spheres, but also the inner (Fig. 2E) of the  $\text{TiO}_2$  hollow spheres, because the large mesopores allow for the diffusion of Fe precursors. Obviously, the heterojunctions are formed between black  $\text{TiO}_2$  and  $\text{M-Fe}_2\text{O}_3$ , which favor the separation of photogenerated charge carriers efficiently. The energy dispersive X-ray (EDS) elemental mappings (Fig. 2G–I) confirm that the Ti, O, and Fe are uniformly distributed in  $\text{M-Fe}_2\text{O}_3/\text{b-TiO}_2$  heterojunctions, indicating the uniform loading of  $\text{M-Fe}_2\text{O}_3$  on mesoporous black  $\text{TiO}_2$  hollow spheres.

The chemical state of each element in composite was studied by X-ray photoelectron spectroscopy (XPS) analysis (Fig. 3A). The full spectrum scan shows the presence of Ti, Fe, C and O peaks in the  $\text{M-Fe}_2\text{O}_3/\text{b-TiO}_2$  heterojunctions, indicating the formation of  $\text{M-Fe}_2\text{O}_3/\text{b-TiO}_2$  composites. The XPS peaks of  $\text{Fe } 2p_{3/2}$  and  $\text{Fe } 2p_{1/2}$  for the  $\text{M-Fe}_2\text{O}_3/\text{b-TiO}_2$  heterojunctions are shown in Fig. 3B. The position of  $\text{Fe } 2p_{3/2}$  is located at 711 eV,  $\text{Fe } 2p_{1/2}$  at 724.6 and 719.3 eV have a distinct satellite peak similar to the reported  $\text{M-Fe}_2\text{O}_3$ , indicating the formation of  $\text{M-Fe}_2\text{O}_3$ . From the  $\text{Fe } 3p$  peak in Fig. S2, it can be deconvoluted into two peaks centered at 56.24 and 54.95 eV, which are assigned to  $\text{Fe}^{3+}$  and  $\text{Fe}^{2+}$ , respectively [34,35]. The presence of  $\text{Fe}^{2+}$  is ascribed to the surface hydrogenation treatment leading to the

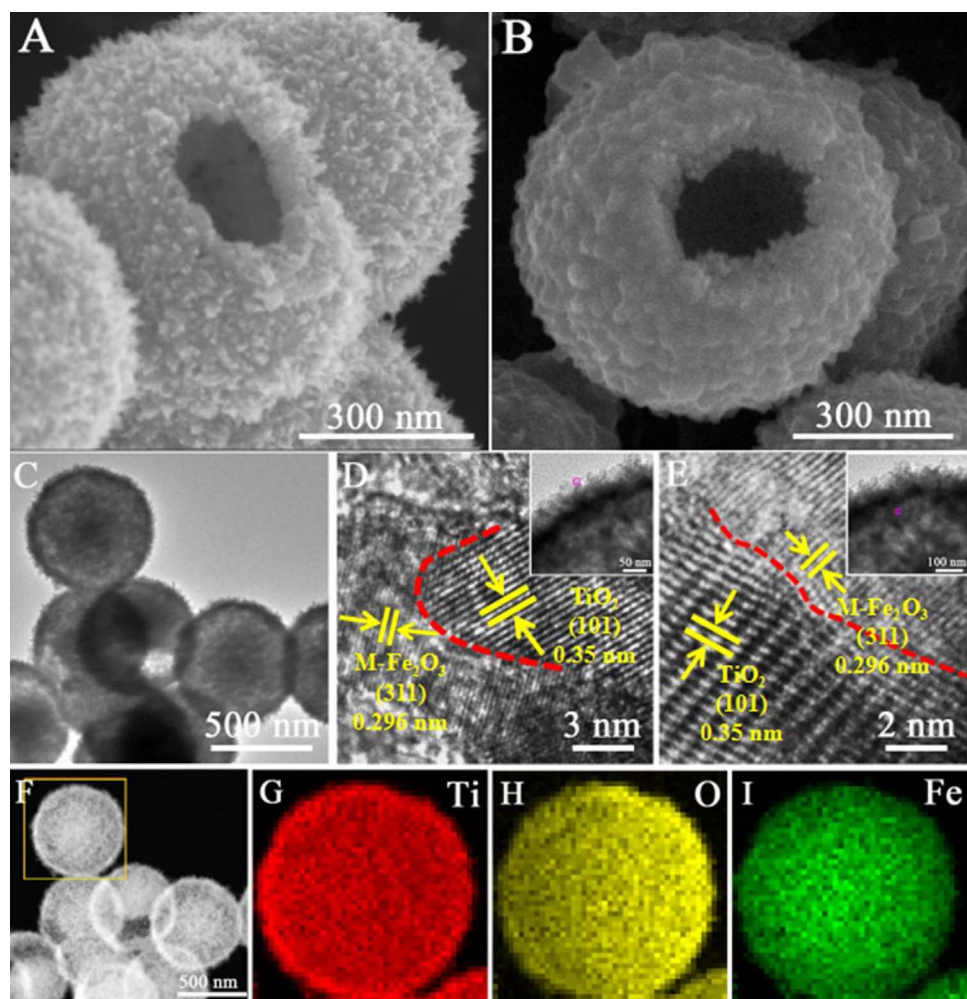


**Fig. 2.** The SEM images of M- $\text{Fe}_2\text{O}_3$ /TiO<sub>2</sub> (A) and M- $\text{Fe}_2\text{O}_3$ /b-TiO<sub>2</sub> (B), the TEM (C), HRTEM images (D,E) and EDS elemental mappings of M- $\text{Fe}_2\text{O}_3$ /b-TiO<sub>2</sub> (F–I).

reduction of parts of  $\text{Fe}^{3+}$  to  $\text{Fe}^{2+}$ . As shown in Fig. 3C, the  $\text{Ti } 2p_{3/2}$  and  $\text{Ti } 2p_{1/2}$  centered at 458.3 and 464.2 eV, are assigned to  $\text{Ti}^{4+}$  of M- $\text{Fe}_2\text{O}_3$ /b-TiO<sub>2</sub> heterojunctions [36]. And two other peaks are located at 457.9 and 463.4 eV, which are consistent with the characteristic of  $\text{Ti } 2p_{3/2}$  and  $\text{Ti } 2p_{1/2}$  peaks for  $\text{Ti}^{3+}$  [37–39]. These peaks transferred to lower binding energy compared to  $\text{Ti}^{4+}$ , indicating a different bonding environment and the presence of  $\text{Ti}^{3+}$  in M- $\text{Fe}_2\text{O}_3$ /b-TiO<sub>2</sub> heterojunctions. The M- $\text{Fe}_2\text{O}_3$ /b-TiO<sub>2</sub> heterojunctions exhibit a wide O 1 s peak with a strong shoulder at a high binding energy (Fig. 3D). This broad peak can be divided into two peaks concentrated at approximately 530.2 and 531.8 eV. The broader peak at 531.8 eV could be attributed to Ti-OH species, implying the formation of more hydroxyl groups on the M- $\text{Fe}_2\text{O}_3$ /b-TiO<sub>2</sub> heterojunctions surface after hydrogen treatment.

### 3.2. Photocatalytic properties

The photocatalytic degradation of MO and high-toxic metribuzin was carried out to evaluate the photocatalytic property of M- $\text{Fe}_2\text{O}_3$ /b-TiO<sub>2</sub> heterojunctions. Fig. 4A shows the photocatalytic degradation performance of MO for M- $\text{Fe}_2\text{O}_3$ /TiO<sub>2</sub> and M- $\text{Fe}_2\text{O}_3$ /b-TiO<sub>2</sub> heterojunctions under AM 1.5 irradiation. The photocatalytic degradation ratio of M- $\text{Fe}_2\text{O}_3$ /b-TiO<sub>2</sub> heterojunctions can be up to 99.8% with 40 min, which is much higher than that of M- $\text{Fe}_2\text{O}_3$ /TiO<sub>2</sub>. The linear relation of  $-\ln(\text{TOC}/\text{TOC}_0)$  for M- $\text{Fe}_2\text{O}_3$ /TiO<sub>2</sub> and M- $\text{Fe}_2\text{O}_3$ /b-TiO<sub>2</sub> heterojunctions can be observed and the linear trend demonstrates that the photocatalytic decomposition of MO under these reaction conditions follows pseudo-first-order kinetics. The first-order rate constants

(k) of M- $\text{Fe}_2\text{O}_3$ /TiO<sub>2</sub>, M- $\text{Fe}_2\text{O}_3$ /b-TiO<sub>2</sub> are 0.021 and 0.077  $\text{min}^{-1}$ , respectively. The k for M- $\text{Fe}_2\text{O}_3$ /b-TiO<sub>2</sub> heterojunctions is about 3 times higher than that of M- $\text{Fe}_2\text{O}_3$ /TiO<sub>2</sub>. The high photocatalytic performance of M- $\text{Fe}_2\text{O}_3$ /b-TiO<sub>2</sub> heterojunctions may be ascribed to the narrow bandgap extending the photoresponse to visible-light and near infrared regions, and the introduction of  $\text{Ti}^{3+}$  promotes the separation of photogenerated electron-hole pairs and accelerates the electron transfer. This is also demonstrated by the photoluminescence (PL) analysis, which is a well-established noncontact technique for the photophysical processes of semiconductors. As can be seen from Fig. S4, the photogenerated electron-hole recombination efficiency of M- $\text{Fe}_2\text{O}_3$ /b-TiO<sub>2</sub> heterojunctions is lower than that of M- $\text{Fe}_2\text{O}_3$ /TiO<sub>2</sub>, suggesting the high-efficient separation of photogenerated charge carriers for the former. Fig. 4B shows the photocatalytic degradation performance of MO for M- $\text{Fe}_2\text{O}_3$ /b-TiO<sub>2</sub> heterojunctions with different loading amounts of M- $\text{Fe}_2\text{O}_3$ . With the increase of M- $\text{Fe}_2\text{O}_3$ , the photocatalytic degradation ratio increased firstly and then decreased. The solar-driven photocatalytic performance for M- $\text{Fe}_2\text{O}_3$ /b-TiO<sub>2</sub> heterojunctions with the loading amount of M- $\text{Fe}_2\text{O}_3$  of ~16 wt.% achieves a maximum. So, the loading amount of M- $\text{Fe}_2\text{O}_3$  is fixed at ~16 wt.% in the following study. In addition, as shown in Fig. S5, the photocatalytic degradation performance of MO for M- $\text{Fe}_2\text{O}_3$ /b-TiO<sub>2</sub> heterojunctions is not only higher than that of M- $\text{Fe}_2\text{O}_3$  and b-TiO<sub>2</sub>, but also higher than that of M- $\text{Fe}_2\text{O}_3$  & b-TiO<sub>2</sub> (the physical mixture of mesoporous black TiO<sub>2</sub> hollow spheres and M- $\text{Fe}_2\text{O}_3$  nanoparticles, referred to as M- $\text{Fe}_2\text{O}_3$  & b-TiO<sub>2</sub>, with a weight ratio of 21:4) and M- $\text{Fe}_2\text{O}_3$ /b-TiO<sub>2</sub> after being crushed. And their k values varied in multiples, as shown in Table S1. It can be attributed to the fact that the physical mixture of M- $\text{Fe}_2\text{O}_3$

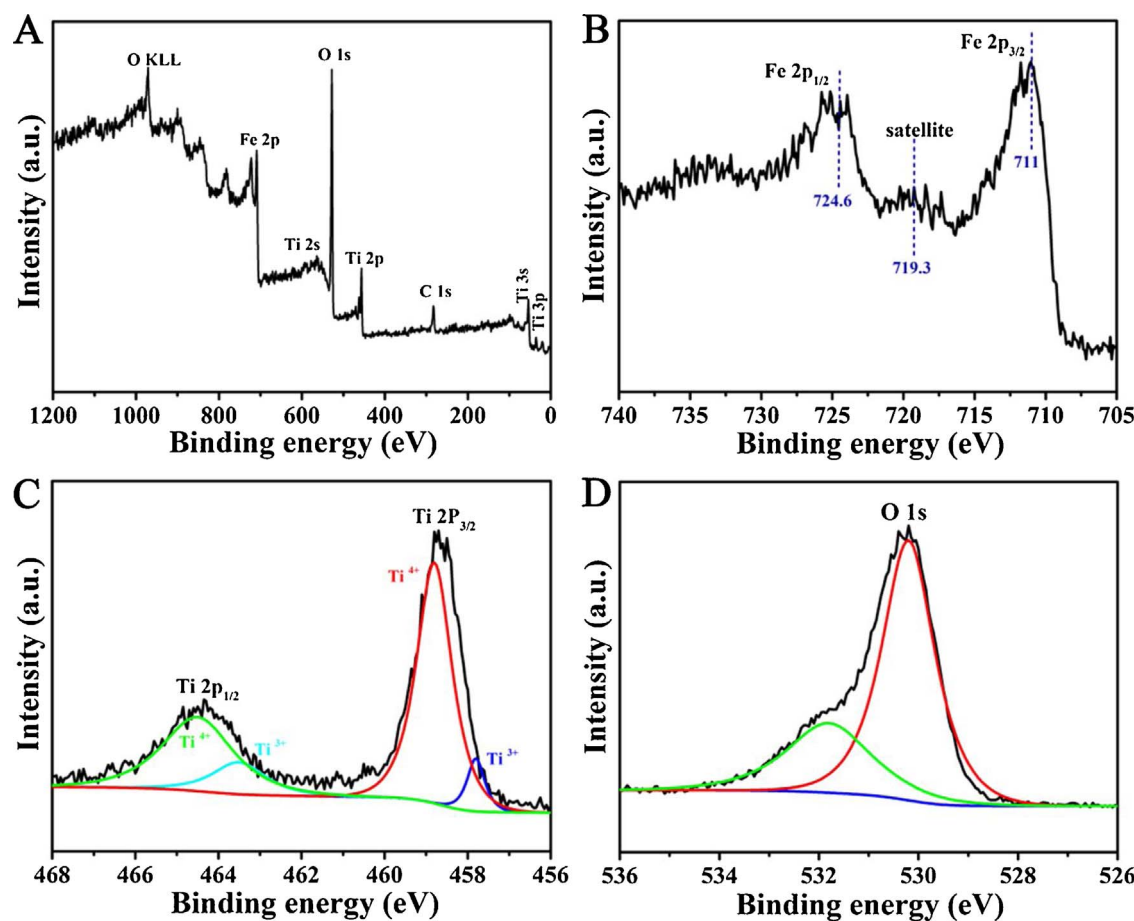
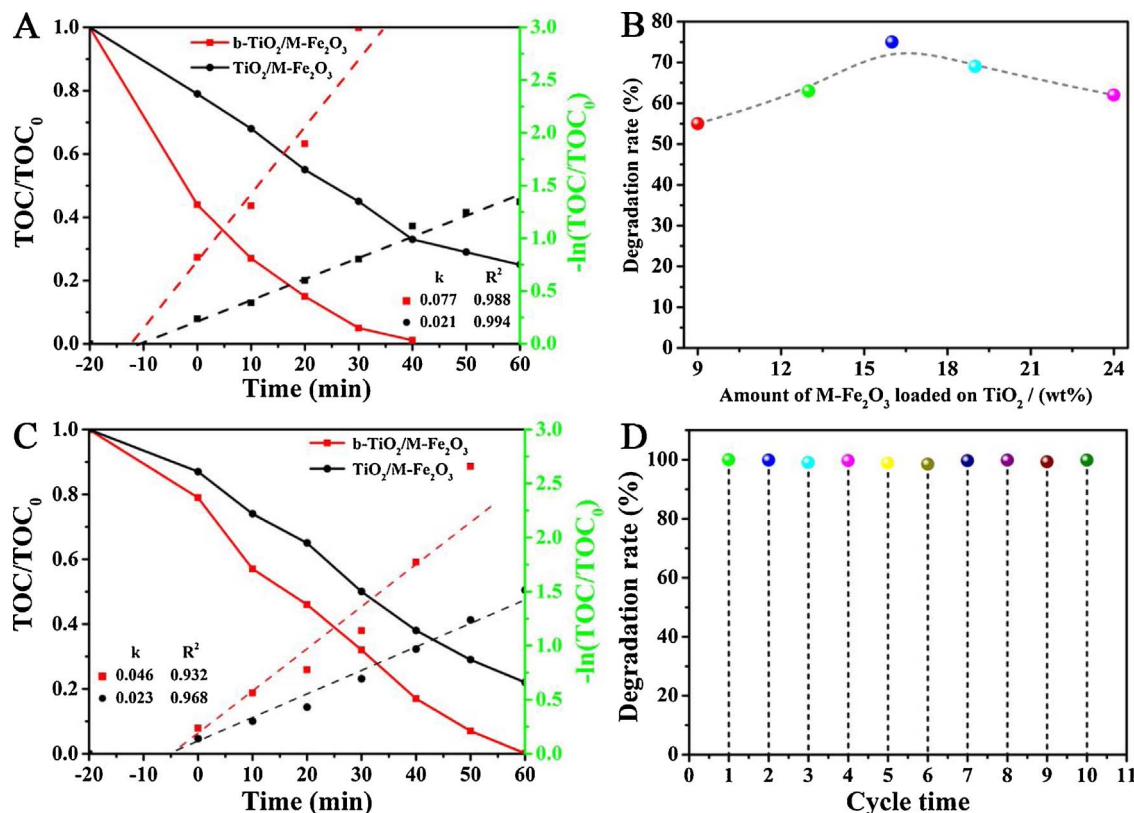


Fig. 3. XPS spectra of the full survey spectrum (A), Fe 2p (B), Ti 2p (C) and O 1 s (D) for M-Fe<sub>2</sub>O<sub>3</sub>/b-TiO<sub>2</sub> heterojunctions, respectively.

nano-particles and TiO<sub>2</sub> hollow spheres results in the poor contact between the two components, which hinders the interface charge transfer. This further confirms that the formation of heterojunctions indeed favor the separation of photogenerated charge carriers. Therefore, in the M-Fe<sub>2</sub>O<sub>3</sub>/b-TiO<sub>2</sub> heterostructures, the M-Fe<sub>2</sub>O<sub>3</sub> nanoparticles is expected to act as an efficient light harvester and the M-Fe<sub>2</sub>O<sub>3</sub>/b-TiO<sub>2</sub> heterostructure provides the efficient charge separation to suppress the electron-hole recombination, which greatly enhances the photocatalytic activity in the photocatalytic degradation. The photocatalytic degradation of M-Fe<sub>2</sub>O<sub>3</sub>/b-TiO<sub>2</sub> heterojunctions is higher than that of M-Fe<sub>2</sub>O<sub>3</sub>/b-TiO<sub>2</sub> after being crushed. The main reason is that the hollow spheres can realize multiple reflections inside the cavity of the hollow spheres, thus improving the utilization rate of light. In order to further evaluate the photocatalytic performance, a colorless organic pesticide metribuzin is adopted as aim contaminants [40,41]. As can be seen from Fig. 4C, the kinetic data can be fitted by pseudo-first-order and the rate of this catalyst performance is calculated by the kinetic equation  $-\ln(\text{TOC}/\text{TOC}_0) = kt$ . The k values are about 0.023 and 0.046 min<sup>-1</sup> for M-Fe<sub>2</sub>O<sub>3</sub>/TiO<sub>2</sub> and M-Fe<sub>2</sub>O<sub>3</sub>/b-TiO<sub>2</sub> heterojunctions under AM 1.5 irradiation, respectively. Obviously, the solar-driven photocatalytic degradation ratio (99% within 60 min) is higher for M-Fe<sub>2</sub>O<sub>3</sub>/b-TiO<sub>2</sub> heterojunctions than that of the pristine one. The magnetic properties would favor the separation and recycle of M-Fe<sub>2</sub>O<sub>3</sub>/b-TiO<sub>2</sub> sample from the aqueous solution by an external magnetic field as shown in Fig. S6. The photocatalysts can be separated easily by a magnet, which favors the recycle of catalysts. After recycle for ten times, the photocatalytic performance of M-Fe<sub>2</sub>O<sub>3</sub>/b-TiO<sub>2</sub> heterojunctions for metribuzin is nearly kept constant, indicating the high stability. Moreover, the photocatalytic degradation performance of metribuzin for M-Fe<sub>2</sub>O<sub>3</sub>/b-TiO<sub>2</sub> heterojunctions has negligible decrease after storing for six months

compared to the fresh one (Fig. S7), further illustrating the high stability of the catalysts, which is favorable for practical applications in environment. In addition, the photocatalytic performance of single wavelength with 365, 420, 520 and 950 nm is also tested in order to investigate the contribution for different wavelength region. From Fig. S8, the b-TiO<sub>2</sub> and M-Fe<sub>2</sub>O<sub>3</sub>/b-TiO<sub>2</sub> heterojunctions both show excellent photocatalytic degradation property under 365 nm irradiation, implying the high utilization ratio of UV region for both of them. The photocatalytic performance decreases sharply under single wavelength of 420 and 520 nm, confirming the main contribution is still UV light. It is worth noting that the photocatalytic performance of metribuzin for M-Fe<sub>2</sub>O<sub>3</sub>/b-TiO<sub>2</sub> heterojunctions is better than that of b-TiO<sub>2</sub> both under 420 and 520 nm. It is about 8 and 9 times higher for M-Fe<sub>2</sub>O<sub>3</sub>/b-TiO<sub>2</sub> heterojunctions than that of b-TiO<sub>2</sub> for 420 and 520 nm, respectively. What's more, for single-wavelength of 950 nm, the photocatalytic degradation ratio of metribuzin for M-Fe<sub>2</sub>O<sub>3</sub>/b-TiO<sub>2</sub> heterojunctions is up to 4%, indicating the efficient utilization of near infrared and confirming the wide-spectrum response due to photothermal effect. The results confirm that the utilization ratio of solar light and the separation efficiency of photogenerated electron-hole pairs are indeed improved significantly due to the formation of heterojunctions and sufficient surface hydrogenation.

As we all know that hydroxyl radical ( $\cdot\text{OH}$ ) is the most important oxidation species in photocatalytic reaction, which plays an important role in organic molecular decomposition. Coumarin as non-fluorescent molecules, can react with  $\cdot\text{OH}$  to generate 7-hydroxycoumarin [42], which has strong fluorescence characteristics, and other active free radicals in solutions, such as  $\text{HO}_2^\bullet$  have no obvious effect on fluorescence intensity. Thus, the coumarin was chosen as a fluorescence probe, for which the fluorescence signal is at approximately 470 nm. As shown



**Fig. 4.** Photocatalytic degradation performances of MO (A) and metribuzin (C) and the corresponding variations in  $-\ln(\text{TOC}/\text{TOC}_0)$  of M-Fe<sub>2</sub>O<sub>3</sub>/TiO<sub>2</sub> and M-Fe<sub>2</sub>O<sub>3</sub>/b-TiO<sub>2</sub> heterojunctions under AM 1.5 irradiation. Photocatalytic degradation MO performance of M-Fe<sub>2</sub>O<sub>3</sub>/b-TiO<sub>2</sub> heterojunctions with different loading amounts of M-Fe<sub>2</sub>O<sub>3</sub> (B) and the recycle of M-Fe<sub>2</sub>O<sub>3</sub>/b-TiO<sub>2</sub> heterojunctions for photodegradation of metribuzin (D). The loading amount of M-Fe<sub>2</sub>O<sub>3</sub> is 16 wt.% for (A), (C) and (D).

In Fig. 5A, significant fluorescence signal can be observed under AM 1.5 irradiation. The fluorescence intensity is increased with increasing the irradiation time. The linear relationship between fluorescence intensity and irradiation time (the inset of Fig. 5A) confirms the high stability of M-Fe<sub>2</sub>O<sub>3</sub>/TiO<sub>2</sub> and M-Fe<sub>2</sub>O<sub>3</sub>/b-TiO<sub>2</sub> heterojunctions. The  $\cdot\text{OH}$  density of M-Fe<sub>2</sub>O<sub>3</sub>/b-TiO<sub>2</sub> heterojunctions is much higher than that of M-Fe<sub>2</sub>O<sub>3</sub>/TiO<sub>2</sub>, which may be the main reason for the high photocatalytic performance of the former. As shown in Fig. 5B, the magnetic properties of M-Fe<sub>2</sub>O<sub>3</sub>/TiO<sub>2</sub> and M-Fe<sub>2</sub>O<sub>3</sub>/b-TiO<sub>2</sub> heterojunctions were measured by the vibrating sample magnetometer (VSM). The M-Fe<sub>2</sub>O<sub>3</sub>/b-TiO<sub>2</sub> heterojunctions and M-Fe<sub>2</sub>O<sub>3</sub>/TiO<sub>2</sub> give typical ferromagnetic behaviors with strong saturation magnetization (Ms) at about 70 and 30 emug<sup>-1</sup>, respectively. The M-Fe<sub>2</sub>O<sub>3</sub>/b-TiO<sub>2</sub> heterojunctions shows a stronger magnetic property than that of the pristine one, which may be ascribed to the reduction of hydrogen treatment. Compared with required for magnetization of the sample data of literatures, the requirements of magnetic separation can be achieved [43,44]. Therefore, to fabricate magnetic composite material provides a more convenient way for the recycle of photocatalysts, and effectively overcome the general slurry TiO<sub>2</sub> catalyst system to repeatedly use. The photoelectrochemical properties of the M-Fe<sub>2</sub>O<sub>3</sub>/b-TiO<sub>2</sub> heterojunctions and M-Fe<sub>2</sub>O<sub>3</sub>/TiO<sub>2</sub> were also performed and shown in Fig. S9. Linear sweeps voltammogram of the M-Fe<sub>2</sub>O<sub>3</sub>/b-TiO<sub>2</sub> heterojunctions shows a photocurrent density of 11.7  $\mu\text{A cm}^{-2}$ , which is almost three times as high as that of the M-Fe<sub>2</sub>O<sub>3</sub>/TiO<sub>2</sub> materials (4.6  $\mu\text{A cm}^{-2}$ ) in 1 M KOH under AM 1.5 irradiation (Fig. S9A). The chronoamperometry responses of both M-Fe<sub>2</sub>O<sub>3</sub>/b-TiO<sub>2</sub> heterojunctions and M-Fe<sub>2</sub>O<sub>3</sub>/TiO<sub>2</sub> materials at 0.6 V are constant (Fig. S9B), indicating their good stabilities. Electrochemical impedance spectroscopy (EIS) was performed to investigate the interface charge separation efficiency for the as-prepared samples in the dark and AM 1.5 irradiation. As shown in Fig. 5C, the resistance values of M-Fe<sub>2</sub>O<sub>3</sub>/b-TiO<sub>2</sub> and M-Fe<sub>2</sub>O<sub>3</sub>/TiO<sub>2</sub> are  $\sim 13.1$  and  $14.5 \Omega$

under AM 1.5 irradiation, respectively. So, the M-Fe<sub>2</sub>O<sub>3</sub>/b-TiO<sub>2</sub> heterojunctions show smaller impedance than that of M-Fe<sub>2</sub>O<sub>3</sub>/TiO<sub>2</sub>, indicating a more efficient charge separation. The M-Fe<sub>2</sub>O<sub>3</sub>/b-TiO<sub>2</sub> heterojunctions and M-Fe<sub>2</sub>O<sub>3</sub>/TiO<sub>2</sub> both show a positive slope in the Mott-Schottky plots (as shown in Fig. 5D), demonstrating n-type semiconductor characteristics. From the plots, the M-Fe<sub>2</sub>O<sub>3</sub>/b-TiO<sub>2</sub> heterojunctions shows a substantially smaller slope than that of M-Fe<sub>2</sub>O<sub>3</sub>/TiO<sub>2</sub>. The carrier density can be calculated from the corresponding slope according to Eq. (1) [45].

$$N_d = \frac{2/e_0 \epsilon \epsilon_0}{d(1/C^2)/dV} \quad (1)$$

We take  $\epsilon = 55$  for anatase TiO<sub>2</sub>. The electron densities of M-Fe<sub>2</sub>O<sub>3</sub>/b-TiO<sub>2</sub> heterojunctions and M-Fe<sub>2</sub>O<sub>3</sub>/TiO<sub>2</sub> are approximately  $4.3 \times 10^{18}$  and  $2.2 \times 10^{18} \text{ cm}^{-3}$ , respectively. The major reasons of the high electron density for M-Fe<sub>2</sub>O<sub>3</sub>/b-TiO<sub>2</sub> heterojunctions are the presence of Ti<sup>3+</sup> in frameworks and the formation of heterojunctions favoring the efficient spatial separation of photogenerated charge carriers. That may be responsible for the high photocatalytic activities of the M-Fe<sub>2</sub>O<sub>3</sub>/b-TiO<sub>2</sub> heterojunctions.

The photocatalytic mechanism is also proposed in this study. By combining the Fermi energy levels of the black TiO<sub>2</sub> hollow spheres and M-Fe<sub>2</sub>O<sub>3</sub> nanoparticles with their bandgap energies and XPS valence-band spectra, the corresponding band structures are established in Fig. 6. The XPS valence-band spectra shown in Fig. S10 indicate that the valence-band maxima (VBM) of the black TiO<sub>2</sub> hollow spheres and M-Fe<sub>2</sub>O<sub>3</sub> nanoparticles after hydrogenation are  $\sim 2.21$  and  $2.41 \text{ eV}$ , respectively. The valence band of M-Fe<sub>2</sub>O<sub>3</sub> is lower than that of black TiO<sub>2</sub>, which favors the photogenerated holes transferring to the valence band of black TiO<sub>2</sub>. As shown in Fig. S11, the optical bandgap of M-Fe<sub>2</sub>O<sub>3</sub> after hydrogenation is  $\sim 2.24 \text{ eV}$ . Obviously, the midgap states between conduction-band minimum (CBM) and VBM are formed for

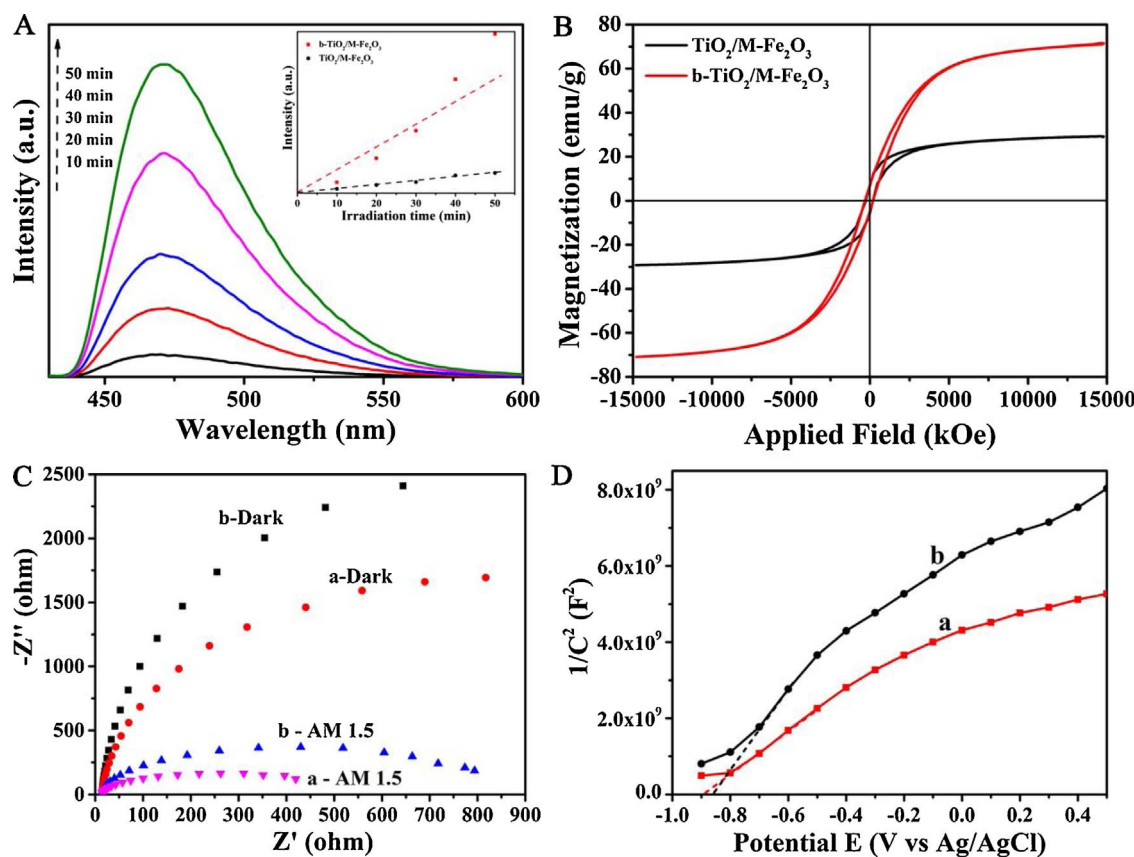


**Fig. 5.** Fluorescence spectra (A) of  $\text{M-Fe}_2\text{O}_3/\text{b-TiO}_2$  heterojunctions under AM 1.5 irradiation. The inset depicts the time dependences of fluorescence intensity at 470 nm. Magnetization hysteresis loops (B), Nyquist plots (C) of electrochemical impedance in the dark and under AM 1.5, and Mott-Schottky plots (D) of  $\text{M-Fe}_2\text{O}_3/\text{b-TiO}_2$  heterojunctions (a) and  $\text{M-Fe}_2\text{O}_3/\text{TiO}_2$  (b), respectively.

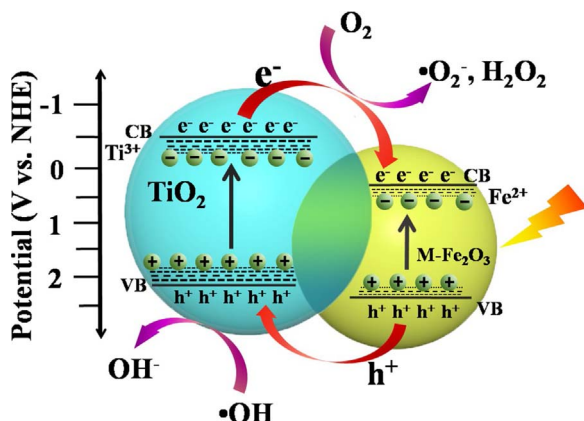


**Fig. 6.** Schematic illustration of the energy band structure for  $\text{M-Fe}_2\text{O}_3/\text{b-TiO}_2$  heterojunctions and the proposed photogenerated charge transfer mechanism.

$\text{TiO}_2$  and  $\text{Fe}_2\text{O}_3$  after surface hydrogenation, because of the formation of oxygen vacancy ( $\text{Ov}$ ),  $\text{Ti}^{3+}$  and  $\text{Fe}^{2+}$ , which narrows the bandgap of  $\text{TiO}_2$  and  $\text{Fe}_2\text{O}_3$  significantly and favors the separation of photo-generated charge carriers. As shown in Fig. 6, the position of the CBM for the black  $\text{TiO}_2$  hollow sphere is higher than that of  $\text{M-Fe}_2\text{O}_3$  nanoparticles, while the VBM for the  $\text{M-Fe}_2\text{O}_3$  nanoparticles is lower than that of the black  $\text{TiO}_2$  hollow sphere. The photocatalytic reaction involves initial absorption of a photon by  $\text{M-Fe}_2\text{O}_3/\text{b-TiO}_2$  heterojunctions photocatalyst in an aqueous medium under sunlight irradiation. A redox reaction is taking place by the photoexcitation of electron from the valence band to the conduction band. Conduction band electrons can be transferred easily by  $\text{TiO}_2$  to its surface and generate an electron deficiency or hole in the valence band. An electron in the  $\text{TiO}_2$  instantly

captures dissolved oxygen in the aqueous medium resulting in the formation of  $\cdot\text{O}_2^-$  radicals and  $\text{H}_2\text{O}_2$  (Fig. S12). Meanwhile, the holes react with water or hydroxide ions, producing  $\cdot\text{OH}$  with strong oxidation ability, which can completely mineralize the organic pollutant.

#### 4. Conclusions

In summary, we have demonstrated wet-impregnation and surface hydrogenation method for the preparation of  $\text{M-Fe}_2\text{O}_3/\text{b-TiO}_2$  heterojunctions. The photoresponse was extended to near infrared region because of the introduction of narrow bandgap  $\text{M-Fe}_2\text{O}_3$  and  $\text{Ti}^{3+}$  species. The  $\text{M-Fe}_2\text{O}_3/\text{b-TiO}_2$  heterojunctions with the loading amount of  $\text{M-Fe}_2\text{O}_3$  of ~16 wt.% exhibited excellent photocatalytic degradation performance and long-term stability for complete mineralization MO and metribuzin. As pseudo-first-order kinetics reaction, the  $k$  for  $\text{M-Fe}_2\text{O}_3/\text{b-TiO}_2$  heterojunctions was about 3 times higher than that of  $\text{M-Fe}_2\text{O}_3/\text{TiO}_2$ . The photocatalytic performance for  $\text{M-Fe}_2\text{O}_3/\text{b-TiO}_2$  heterojunctions under single wavelength with 365, 420, 520 and 950 nm irradiation, was much higher than that of  $\text{b-TiO}_2$ . This was ascribed to the narrow bandgap extending the photoresponse to visible-light and near infrared regions, and the formation of heterojunctions and introduction of  $\text{Ti}^{3+}$  promoted the separation of photogenerated electron-hole pairs and accelerated the electron transfer. Moreover, the photocatalysts could be separated easily by a magnet, which favored the recycle of catalysts in practical applications. This strategy provides new insights for the design of recyclable and high-efficiency photocatalysts for environmental remediation.

#### Competing financial interests

The authors declare no competing financial interests.

## Acknowledgments

We gratefully acknowledge the support of the Key Program Projects of the National Natural Science Foundation of China (21631004), the National Natural Science Foundation of China (21371053, 21376065, 51672073, 21771059), the Natural Science Foundation of Heilongjiang Province (B2017008) and the University Nursing Program for Young Scholars with Creative Talents in Heilongjiang Province (UNPYSCT-2015014).

## Appendix A. Supplementary data

Supplementary data associated with this article can be found, in the online version, at <http://dx.doi.org/10.1016/j.apcatb.2017.09.023>.

## References

- [1] C. Boerigter, R. Campana, M. Morabito, S. Linic, *Nat. Commun.* 7 (2016) 5414–5445.
- [2] D. Schultz, T. Yoon, *Science* 343 (2014) 985–993.
- [3] C. Yu, G. Li, S. Kumar, K. Yang, R. Jin, *Adv. Mater.* 26 (2014) 892–898.
- [4] F. Brandl, N. Bertrand, E. Lima, *Nat. Commun.* 6 (2015) 7765.
- [5] T. Le, D. Flahaut, H. Martinez, H. Nguyen, T. Huynh, *Appl. Catal. B: Environ.* 165 (2015) 260–268.
- [6] A. Dhakshinamoorthy, A. Asiri, H. Garcia, *Angew. Chem. Int. Ed.* 55 (2016) 5414–5445.
- [7] W. Dong, Y. Sun, W. Hua, Y. Yao, G. Zhuang, X. Lv, Q. Ma, D. Zhao, *Adv. Funct. Mater.* 26 (2016) 964–976.
- [8] R. Asahi, T. Morikawa, T. Ohwaki, K. Aoki, Y. Taga, *Science* 293 (2001) 269–271.
- [9] Y. Xu, C. Zhang, P. Lu, X. Zhang, L. Zhang, J. Shi, *Nano Energy* 38 (2017) 494–503.
- [10] X. Zheng, G. Shen, C. Wang, Y. Li, D. Dunphy, T. Hasan, C. Brinker, B. Su, *Nat. Commun.* 8 (2017) 14921.
- [11] S. Ma, S. Zhan, Y. Jia, Q. Shi, Q. Zhou, *Appl. Catal. B: Environ.* 186 (2016) 77–87.
- [12] K. Ji, J. Deng, H. Zang, J. Han, H. Arandiyani, H. Dai, *Appl. Catal. B: Environ.* 165 (2015) 285–295.
- [13] M. Ruokolainen, E. Ollikainen, T. Sikanen, T. Kotiaho, R. Kostiainen, *J. Am. Chem. Soc.* 138 (2016) 7452–7455.
- [14] Y. Liu, N. Liu, Y. Han, X. Zhang, H. Huang, Y. Lifshitz, S. Lee, J. Zhong, Z. Kang, *Science* 347 (2015) 970–974.
- [15] X. Gan, M. Meng, X. Zhu, L. Yang, P. Chu, *ACS Nano* 8 (2014) 9304–9310.
- [16] L. Zhu, L. Wang, N. Bing, C. Huang, L. Wang, G. Liao, *ACS Appl. Mater. Interfaces* 5 (2013) 12478–12487.
- [17] W. Guo, F. Zhang, C. Lin, Z. Wang, *Adv. Mater.* 24 (2012) 4761–4764.
- [18] S. Selcuk, A. Selloni, *Nat. Mater.* 15 (2016) 1107–1112.
- [19] Y. Deng, M. Xing, J. Zhang, *Appl. Catal. B: Environ.* 211 (2017) 157–166.
- [20] H. Liu, J. Joo, M. Dahl, L. Fu, Z. Zeng, Y. Yin, *Energy Environ. Sci.* 8 (2015) 286–296.
- [21] X. Chen, L. Liu, P. Yu, S. Mao, *Science* 331 (2011) 746–750.
- [22] W. Zhou, W. Li, J. Wang, Y. Qu, Y. Yang, Y. Xie, K. Zhang, L. Wang, H. Fu, D. Zhao, *J. Am. Chem. Soc.* 136 (2014) 9280–9283.
- [23] G. Wang, H. Wang, Y. Ling, Y. Tang, X. Yang, R. Fitzmorris, C. Wang, J. Zhang, Y. Li, *Nano Lett.* 11 (2011) 3026–3033.
- [24] M. Islam, H. Kim, D. Reddy, Y. Kim, R. Ma, H. Baek, J. Kim, T. Kim, *Dalton Trans.* 46 (2017) 6013–6023.
- [25] K. Li, Z. Zeng, L. Yan, M. Huo, Y. Guo, S. Luo, X. Luo, *Appl. Catal. B: Environ.* 187 (2016) 269–280.
- [26] A. Banisharif, A. Khodadadi, Y. Mortazavi, A. Firooz, J. Beheshtian, S. Agah, S. Menbari, *Appl. Catal. B: Environ.* 165 (2015) 209–221.
- [27] W. Subramonian, T. Wu, S. Chai, *J. Environ. Manag.* 187 (2017) 298–310.
- [28] K. Christoforidis, T. Montini, E. Bontempi, S. Zafeiratos, J. Jaén, P. Fornasiero, *Appl. Catal. B: Environ.* 187 (2016) 171–180.
- [29] F. Mou, L. Xu, H. Ma, J. Chen, D. Chen, S. Wang, *Nanoscale* 4 (2012) 4560–4657.
- [30] Q. Wang, N. Zhu, E. Liu, C. Zhang, J. Crittenden, Y. Zhang, Y. Cong, *Appl. Catal. B: Environ.* 205 (2017) 347–356.
- [31] S. Mirmasoomi, M. Mohsen, G. Mona, *Sep. Purif. Technol.* 175 (2017) 418–427.
- [32] W. Hu, W. Zhou, K. Zhang, X. Zhang, L. Wang, B. Jiang, G. Tian, D. Zhao, H. Fu, J. Mater. Chem. A 4 (2016) 7495–7502.
- [33] B. Roose, S. Pathak, U. Steiner, *Chem. Soc. Rev.* 44 (2015) 8326–8349.
- [34] T. Yamashita, P. Hayes, *Appl. Surf. Sci.* 254 (2008) 2441–2449.
- [35] G. Abreu, R. Paniago, H. Pfannes, J. Magn. Magn. Mater. 349 (2014) 235–239.
- [36] A. Danon, K. Bhattacharyya, B.K. Vijayan, J. Lu, D.J. Sauter, K.A. Gray, P.C. Stair, E. Weitz, *ACS Catal.* 2 (2012) 45–49.
- [37] L. Liu, P. Yu, X. Chen, S. Mao, D. Shen, *Phys. Rev. Lett.* 111 (2013) 065505.
- [38] X. Chen, D. Zhao, K. Liu, C. Wang, L. Liu, B. Li, Z. Zhang, D. Shen, *ACS Appl. Mater. Interfaces* 7 (2015) 16070–16077.
- [39] M. Mehta, N. Kodan, S. Kumar, A. Kaushal, L. Mayrhofer, M. Walter, M. Moseler, A. Dey, J. Mater. Chem. A 4 (2016) 2670–2681.
- [40] N. Vela, J. Fenoll, I. Garrido, G. Navarro, M. Gambín, S. Navarro, *Catal. Today* 252 (2015) 70–77.
- [41] M. Antonopoulou, I. Konstantinou, *J. Photochem. Photobiol. A* 294 (2014) 110–120.
- [42] G. Louit, S. Foley, J. Cabillic, H. Coffigny, F. Taran, A. Valleix, J. Renault, S. Pin, *Radiat. Phys. Chem.* 72 (2005) 119–124.
- [43] S. Mirmasoomi, M. Mehdipour Ghazi, M. Galedari, *Sep. Purif. Technol.* 175 (2017) 418–427.
- [44] X. Jia, R. Dai, D. Lian, S. Han, X. Wu, H. Song, *Appl. Sur. Sci.* 392 (2017) 268–276.
- [45] C. Mao, F. Zuo, Y. Hou, X. Bu, P. Feng, *Angew. Chem. Int. Ed.* 53 (2014) 10485–10489.